Received: 17 July 2023 | Revised: 2 April 2024 | Accepted: 21 April 2024

DOI: 10.1002/mp.17112

RESEARCH ARTICLE

MEDICAL PHYSICS

Noise power spectrum (NPS) in computed tomography: Enabling local NPS measurement without stationarity and ergodicity assumptions

Chengzhu Zhang[1] | **Ke Li**[1,2] | **Ran Zhang**[1] | **Guang-Hong Chen**[1,2]

[1]Department of Medical Physics, University of Wisconsin School of Medicine and Public Health, Madison, Wisconsin, USA

[2]Department of Radiology, University of Wisconsin School of Medicine and Public Health, Madison, Wisconsin, USA

Correspondence
Guang-Hong Chen, Department of Medical Physics and Department of Radiology, School of Medicine and Public Health, University of Wisconsin-Madison, Madison, WI 53705, USA.
Email: gchen7@wisc.edu

Funding information
NIH, Grant/Award Numbers: R01EB034011, R01EB032474, R01HL153594; GE Healthcare; Wisconsin Alumni Research Foundation

Abstract

Background: Conventional methods for estimating the noise power spectrum (NPS) often necessitate multiple computed tomography (CT) data acquisitions and are required to satisfy stringent stationarity and ergodicity conditions, which prove challenging in CT imaging systems.

Purpose: The aim was to revisit the conventional NPS estimation method, leading to a new framework that estimates local NPS without relying on stationarity or ergodicity, thus facilitating experimental NPS estimations.

Methods: The scientific foundation of the conventional CT NPS measurement method, based on the Wiener-Khintchine theorem, was reexamined, emphasizing the critical conditions of stationarity and ergodicity. This work proposes an alternative framework, characterized by its independence from stationarity and ergodicity, and its ability to facilitate local NPS estimations. A spatial average of local NPS over a Region of Interest (ROI) yields the conventional NPS for that ROI. The connections and differences between the proposed alternative method and the conventional method are discussed. Experimental studies were conducted to validate the new method.

Results: (1) The NPS estimated using the conventional method was demonstrated to correspond to the spatial average of pointwise NPS from the proposed NPS estimation framework. (2) The NPS estimated over an ROI with the conventional method was shown to be the sum of the NPS estimated from the proposed method and a contribution from measurement uncertainty. (3) Local NPS estimations from the proposed method in this work elucidate the impact of surrounding image content on local NPS variations.

Conclusion: The NPS estimation method proposed in this work allows for the estimation of local NPS without relying on stationarity and ergodicity conditions, offering local NPS estimations with significantly improved precision.

KEYWORDS
local image quality, noise power spectrum, task-specific

1 | INTRODUCTION

1.1 | Notion of signal and noise power

In physics, the instantaneous power absorbed by a load of resistance R in an electrical circuit is given by $|I(t)|^2R$ or $|U(t)|^2/R$, where $I(t)$ and $U(t)$ represent the instantaneous current and voltage, respectively.[1] Consequently, $|I(t)|^2$ and $|U(t)|^2$ represent the instantaneous power absorbed by a unit resistance in a circuit. In contemporary signal processing theory,[2] this concept of the instantaneous power of electrical signals, $I(t)$ and $U(t)$, has been extended to any arbitrary time-varying continuous signal $S(t)$. The instantaneous signal power is therefore defined as the squared modulus of the signal, $|S(t)|^2$.

On the other hand, the current and voltage of an electrical circuit undergo spontaneous fluctuations, or noise, due to thermal agitations and intrinsic quantum fluctuations of the charge carriers.[3–6] For the noise component,[5,6] the instantaneous noise power is defined as $|\Delta S(t)|^2 = |S(t) - \mathbf{E}[S(t)]|^2$, where $\mathbf{E}[S(t)]$ denotes the mathematical expectation of the random variable $S(t)$ at time t. However, both the signal and noise power defined in this way are stochastic quantities and thus their experimentally measured values can only be meaningful in the statistical average sense. This results in the study of their expected values, denoted as $\mathbf{E}[S^2(t)]$ for signal power and $\mathbf{E}[|\Delta S(t)|^2] \equiv \sigma_S^2(t)$ for noise power, respectively. Note that $\mathbf{E}[|\Delta S(t)|^2] \equiv \sigma_S^2(t)$ is nothing but the variance at time point t.

However, for stochastic physical quantities,[7] it is often more insightful to study how the signal and noise at one time point, t_1, impact their properties at a later time point, $t_2 = t_1 + \Delta t$. This leads to the study of the auto-covariance,[8] covariance (COV), of the signal $S(t)$ defined as follows:

$$\mathrm{COV}(t_1, t_2) =: \mathbf{E}([S(t_1) - \mathbf{E}[S(t_1)]][S(t_2) - \mathbf{E}[S(t_2)]]). \quad (1)$$

Taylor introduced this notion in 1922 to characterize the stochastic nature of the time-varying signals.[8] A non-vanishing auto-covariance describes the correlation between the noise at one time point and the noise at a subsequent time point. When $\Delta t \to 0$, the auto-covariance mentioned above converges to the variance at time t_1.

The notions of signal power and noise power have also been generalized to spatially varying signals in the field of medical imaging.[9,10] For a two-dimensional (2D) image slice or a three-dimensional (3D) image volume, power is defined as the square of the absolute value. The total signal and noise energy is given by the integral across all spatial dimensions, thereby offering a measure of the total signal power throughout the entire image slice or image volume. Similarly, the study of signal and noise power spectral (NPS) analyses has become an integral component of contemporary medical imaging physics as it delivers the requisite insight into the imaging system, leading to further optimizations for improved imaging performance.[11–48] An example of this would be the optimization of computed tomography (CT) imaging systems that mitigate noise, thereby facilitating low radiation dose CT imaging.

1.2 | Spectral analysis methods for signal power and noise power

Instead of evaluating signal and noise power in the time domain or spatial domain, where data acquisition typically occurs, Fourier analysis can be applied to decompose these powers into contributions from each temporal or spatial frequency, namely, the power spectrum. This power spectrum is instrumental in understanding the influence of noise on the signal and its frequency-dependent variations. Introducing Fourier spectrum analysis to functions defined for the covariance function (see Equation (1) or its spatial generalizations) is mathematically nontrivial. Wiener[49] pioneered this approach with his generalized harmonic analysis, addressing the existence and convergence of the Fourier transform for relatively simpler deterministic functions. Khintchine[50] later extended this approach to stochastic processes. While these intricate details are often overlooked in applied fields, as in this paper, their significance cannot be understated.

In the following subsection, we briefly review these two foundational frameworks and their interconnections. Subsequently, we will introduce our framework for pointwise NPS analysis, which diverges from the traditional stationarity and ergodicity conditions of Wiener and Khintchine's methodologies.

1.3 | Brief review of Wiener's spectral analyses for deterministic signals

Wiener[49] introduced a generalized harmonic analysis method to discuss the power spectrum of any deterministic time-varying signals. Specifically, for a deterministic signal $S(t)$, Wiener defined the following autocorrelation function:

$$R_S^W(t, \tau) = \frac{1}{2T}\int_{-T}^{+T} dt\, S(t)S(t+\tau) \quad (2)$$

This function characterizes the correlation between a segment of the time-varying signal $S(t)$ over a time window $[-T, +T]$ and the same signal segment, but delayed by time τ, that is, $S(t+\tau)$. It is crucial to note that this autocorrelation represents an average of the

quantity $S(t)S(t+\tau)$ over the time window $[-T, +T]$, characterizing the autocorrelation of the signal $S(t)$ up to a "temporal resolution" of $2T$. This explains the intrinsic dependence of Wiener's autocorrelation function on the time window location, t, and the "resolution" specified by $2T$, making it quasi-local and shift-variant. To eliminate this shift variance, Wiener imposed the shift-invariance condition on the signal, such that $R_S^W(t,\tau) = R_S^W(\tau)$ to facilitate mathematical discussion. The Wiener spectrum of the deterministic signal $S(t)$ under this stationarity condition is given as:

$$\widetilde{R_S^W}(\omega) = \int_{-\infty}^{+\infty} d\tau\, R_S^W(\tau) e^{-i2\pi\omega\tau}. \tag{3}$$

It is important to note that this conceptual framework was developed for deterministic signals, not for stochastic signals.

1.4 | Brief review of Khintchine's spectral analyses for stochastic signals

Following Wiener's development, Khintchine[50] extended this spectral analysis method to stochastic processes, leading to the modern noise power analysis method.[8,50,51] In Khintchine's framework for stochastic signals, the starting point is the auto-covariance, $\mathrm{COV}(t, t+\Delta t)$, defined as the mathematical expectation $\mathbb{E}[\cdot]$:

$$R_S^K(t,\Delta t) =: \mathbb{E}[S(t)S(t+\Delta t)]. \tag{4}$$

This mathematical expectation, contrasting with Wiener's autocorrelation in Equation (2), averages over all possible states of the stochastic signal $S(t)$, making it local to the temporal points t and $t+\Delta t$. Similar to Wiener's function, Khintchine's auto-covariance is inherently shift-variant. In order to advance mathematical formulations, Khintchine introduced the concept of stationarity in stochastic processes, analogous to the principle of shift-invariance in deterministic signals. Under this condition, if the noise is stationary,[7] the auto-covariance function is solely dependent on the time shift Δt and is independent of the specific time t, that is,

$$R_S^K(t,\Delta t) = R_S^K(\Delta t). \tag{5}$$

Under this condition, Khintchine naturally adopted Fourier analysis to define the spectrum of the shift-invariant auto-covariance:

$$\widetilde{R_S^K}(\omega) = \int_{-\infty}^{+\infty} d(\Delta t)\, R_S^K(\Delta t) e^{-2\pi i\omega\Delta t}. \tag{6}$$

Up to this point, Wiener's framework applies to deterministic signals, while Khintchine's framework addresses stochastic signals, with no direct connection between the two.

1.5 | Connection between Wiener's spectral analyses for deterministic signals and Khintchine's spectral analyses for stochastic signals: Wiener-Khintchine theorem

If we notice that a specific realization of the stochastic signal $S(t)$ from the stochastic process can be treated as a deterministic, time-varying signal, then Wiener's autocorrelation function and the associated spectral analysis become applicable to this particular realization of the stochastic process. The immediate question, however, is how to interpret and understand the power spectrum obtained from this specific realization of the stochastic process. It might initially seem that the temporal average in Wiener's framework could be achieved by averaging the local spectrum, as defined in Khintchine's framework, over the time window $[-T, +T]$. This idea is certainly intriguing, but it raises two fundamental questions: (1) Under the stationarity condition for the stochastic process and shift-invariance for the specific realization of the stochastic process, is there any relationship between the Fourier transform $\widetilde{R_S^K}(\omega)$ as per Khintchine and the Fourier transform $\widetilde{R_S^W}(\omega)$, as defined by Wiener? (2) In the context of Khintchine's framework, where does the statistical ensemble average (indicated by the mathematical expectation) fit if there is indeed a connection between these two distinctively defined spectra? Answers to these questions are highly non-trivial. As it turned out that there is indeed a profound link between the time-average integral in Wiener's autocorrelation definition in Equation (2) and the ensemble average of the stochastic quantities in Khintchine's framework. This connection, however, is contingent upon an additional condition of ergodicity being imposed on the stochastic processes.

Under the ergodicity condition, all possible stochastic states of the stochastic variable will be accessed as the time window width T goes to infinity, and thus the time average in Wiener's autocorrelation definition becomes equivalent to the ensemble average over all possible states of Khintchine's stochastic signals. As a result, under both stationarity and ergodicity, one obtains this bizarre yet profound connection:

$$\widetilde{R_S^K}(\omega) = \widetilde{R_S^W}(\omega), \tag{7}$$

which is the central statement of the so-called Wiener-Khintchine theorem.

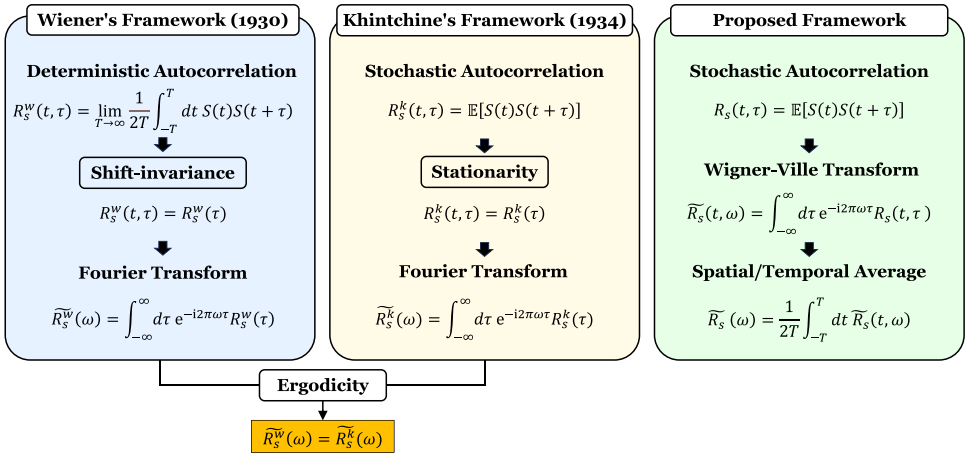

FIGURE 1 Connections between Wiener's signal power spectral analysis framework for deterministic signals and Khintchine's framework for stochastic signals. Both frameworks impose their corresponding stationarity, that is, shift-invariance, conditions to facilitate discussion. The profound connection between the two frameworks was established through the limit of $T \to \infty$ in Wiener's framework and under the ergodicity condition of the stochastic process in Khintchine's framework. In contrast, the proposed framework in this work is also presented in this figure to highlight that neither stationarity nor ergodicity conditions are introduced in the proposed framework.

Note that, in the limit as $T \to \infty$ and under the condition of shift invariance, it is straightforward to demonstrate the following result:

$$\begin{aligned}\widetilde{R_S^W}(\omega) &= \int_{-\infty}^{+\infty} d\tau\, R_S^W(\tau) e^{-i2\pi\omega\tau},\\ &= \lim_{T\to\infty}\left|\frac{1}{2T}\int_{-T}^{T} dt\, S(t)e^{-i2\pi\omega t}\right|^2,\\ &= \left|\tilde{S}(\omega)\right|^2. \end{aligned} \tag{8}$$

When this result is combined with the Wiener-Khintchine theorem, as indicated in Equation (7), one concludes that Khintchine's power spectrum of the stochastic signal, defined as the Fourier transform of the ensemble average of the stochastic quantity $S(t)S(t+\tau)$, can be obtained by taking the infinite time window limit (i.e., $T \to \infty$) of the Fourier transform of a single realization of the stochastic signal $S(t)$ over the finite window $2T$.

When the stochastic signal $S(t)$ is subtracted by its corresponding expected values, $\mathbb{E}[S(t)]$, the concept of auto-correlation changes to the corresponding auto-covariance, as defined in Equation (1). Consequently, the signal spectra transform into the corresponding NPS. For clarity, let's summarize the results of the Wiener-Khintchine theorem (i.e., Equations (7) and (8)) when applied to the auto-covariance as follows: Under stationarity and ergodicity conditions, the Wiener-Khintchine theorem leads to the following NPS estimation method:

$$\begin{aligned}\widehat{\mathrm{NPS}_S^K}(\omega) &= \int_{-\infty}^{+\infty} d\tau\, \mathrm{COV}_S(t, t+\tau) e^{-i2\pi\omega\tau},\\ &= \lim_{T\to\infty}\left|\frac{1}{2T}\int_{-T}^{T} dt\, \Delta S(t) e^{-i2\pi\omega t}\right|^2,\\ &= \left|\widetilde{\Delta S}(\omega)\right|^2. \end{aligned} \tag{9}$$

that is, the NPS can be obtained by taking the squared modulus of the Fourier transform of the "noise" associated with the measured signal, denoted as $\Delta S(t) = S(t) - \mathbb{E}[S(t)]$, over a $2T$-temporal window. The connections between Wiener's power spectral analysis framework for deterministic signals and Khintchine's NPS framework are summarized in Figure 1, contrasting the proposed local NPS analysis method discussed in the next section.

1.6 | Conventional NPS estimation method of x-ray CT image slices recommended by ICRU

To analyze the NPS of a 2D image slice, the method based on the Wiener-Khintchine theorem for NPS measurement, as dictated by Equation (9), is generalized from one temporal domain to spatial domain. This generalization resulted in the NPS estimation method recommended by the International Commission on Radiation Units and Measurements (ICRU) for x-ray CT imaging. The method involves first applying the Fourier transform to the estimated noise-only image, and then computing the squared modulus of the Fourier transform to estimate the NPS for a chosen spatial Region Of Interest (ROI)[32,33]:

$$\widehat{\mathrm{NPS}}^{\mathrm{ICRU}}\left(\vec{k}\right) = \frac{1}{AK}\sum_{j=1}^{K}\left|\mathrm{FT}_{2D}[\Delta\hat{I}^{(j)}(\vec{x})]\right|^2, \tag{10}$$

where A represents the area of the chosen ROI. In the above ICRU-recommended NPS estimation method, a total of K repeated data acquisitions are assumed. The purposes of using K repeated acquisitions in the above ICRU-recommended NPS estimation method are twofold: (1) The sample mean over these K acquisitions can be taken and then used as the estimate of the needed mathematical expectation of the signal, that is, image $\mathbb{E}[I(\vec{x})]$, since this is needed as indicated in Equation (9) to estimate noise $\Delta I(\vec{x}) = I(\vec{x}) - \mathbb{E}[I(\vec{x})]$. (2) An arithmetic average over the obtained NPS from each acquisition, that is, $\frac{1}{K}\sum_{j=1}^{K} |\cdot|^2$, is taken to suppress the excessive measurement uncertainty from a single acquisition. This ICRU recommended method is referred to as the "conventional method" in the remainder of the paper. It is important to emphasize that this method is based on the Wiener-Khintchine theorem, and thus one needs to impose some form of stationarity and also ergodicity to justify its applicability in practice.

2 | PROPOSED LOCAL NPS WITHOUT STATIONARITY AND ERGODICITY CONDITIONS

2.1 | Proposed definition of local NPS beyond stationarity and ergodicity constraints

In this work, we heuristically introduce a windowed Fourier transform for Khintchine's covariance of spatially varying signals, specifically for CT images $I(\vec{x})$, without delving into potential mathematical subtleties such as the existence and convergence of the Fourier transforms. The windowed Fourier transform is defined as follows:

$$C_{II}(\vec{x}_1, \vec{x}_2) := \mathbb{E}\big([I(\vec{x}_1) - \mathbb{E}[I(\vec{x}_1)]][I(\vec{x}_2) - \mathbb{E}[I(\vec{x}_2)]]\big), \quad (11)$$

$$\widetilde{C}_{II}(\vec{k}, \vec{x}_1) = \int_{\Delta\vec{x}\in \mathrm{ROI}} d(\Delta\vec{x})\, C_{II}(\vec{x}_1, \vec{x}_1 + \Delta\vec{x}) e^{-2\pi i \vec{k}\cdot\Delta\vec{x}}. \quad (12)$$

Here, $\vec{x}$ denotes a spatial point and $\Delta\vec{x} = \vec{x}_2 - \vec{x}_1$ represents the distance between two spatial locations. The term ROI refers to the ROI of the image function in the spatial domain, and $\vec{k}$ denotes the spatial frequency vector in a 2D image slice or 3D image volume of $I(\vec{x})$.

Compared with the NPS measurement method recommended by the ICRU, our proposed framework exhibits two key differences. First, we employ the windowed partial Fourier transform (also known as the Wigner-Ville transform in physics and signal processing), defined over an ROI centered around the pivot pixel labeled by $\vec{x}_1$. Unlike in Khintchine's work, we do not impose stationarity conditions. Second, we define the local NPS at location $\vec{x}_1$ as this partial Fourier transform taken over an ROI:

$$\mathrm{NPS}(\vec{k}, \vec{x}_1) := \widetilde{C}_{II}(\vec{k}, \vec{x}_1). \quad (13)$$

The key question is how to estimate this local NPS from experimental data. This task essentially involves the experimental estimation of the covariance $C_{II}(\vec{x}_1, \vec{x}_2)$ as outlined in Equation (11). There are two general strategies to achieve this: one is to estimate the covariance in the reconstructed image domain (referred to as the image-domain method), and the other is to reconstruct the covariance from the estimated noise variance of the projection data (referred to as the projection-domain method). As will be shown in the next subsection, the first strategy is used in the NPS estimation method recommended by the ICRU, which leads to the spatially averaged NPS over an ROI. In contrast, the second strategy is adopted in this paper to enable local NPS estimations.

2.2 | Projection-domain method to estimate covariance $C_{II}(\vec{x}_1, \vec{x}_2)$

The noise in the reconstructed CT images is derived from the noise present in the acquired line integral sinogram projection data. As shown by Wunderlich and Noo[23] and Zhang et al.,[52] due to the linearity of the filtered backprojection (FBP) reconstruction method, the digitized version of the FBP reconstruction can be expressed as follows:

$$\hat{I}(\vec{x}) = \sum_{d,v} \lambda_{d,v}(\vec{x})\hat{p}_{d,v}. \quad (14)$$

Here, $I(\vec{x})$ represents the image value at location $\vec{x}$, $\hat{p}_{d,v} = \ln \frac{\bar{N}_{0;(d,v)}}{N_{(d,v)}}$ denotes the estimated line integral projection data from a single acquisition. In this expression, the photon counts, $N_{(d,v)}$, follow the Poisson distribution, and v and d correspond to it corresponds to view angle index and detector index, respectively, in a single CT data acquisition. On the other hand, $\bar{N}_{0;(d,v)}$ represents the averaged photon flux from the air scan and is therefore a deterministic quantity. $\hat{I}(\vec{x})$ is a random variable and its statistical properties are determined by the statistical properties of the estimated projection data $\hat{p}_{d,v}$. To facilitate the discussion, we further simplify Equation (14) by using a single index m:

$$\hat{I}(\vec{x}) = \sum_{m=1}^{M} \lambda_m(\vec{x})\hat{p}_m. \quad (15)$$

Here $M = D \times V$ represents the total number of measured data points in the sinogram. Correspondingly, the difference image $\Delta I(\vec{x}) = \hat{I}(\vec{x}) - \bar{I}(\vec{x})$ can be expressed in

terms of the difference in sinogram data as follows:

$$\Delta\hat{I}(\vec{x}) = \sum_{m=1}^{M} \lambda_m(\vec{x})\Delta\hat{p}_m. \tag{16}$$

Therefore, it is straightforward to show the covariance $C_{II}(\vec{x}_i, \vec{x}_j)$ for the image noise $\Delta\hat{I}(\vec{x})$ at two spatial locations $\vec{x}_i$ and $\vec{x}_j$ are given as below:

$$\begin{aligned} C_{II}(\vec{x}_i, \vec{x}_j) &= \mathbb{E}[\Delta\hat{I}(\vec{x}_i)\Delta\hat{I}(\vec{x}_j)], \\ &= \sum_{m,m'=1}^{M} \lambda_m(\vec{x}_i)\lambda_{m'}(\vec{x}_j)\mathbb{E}[\Delta\hat{p}_m\Delta\hat{p}_{m'}], \\ &= \sum_{m,m'=1}^{M} \lambda_m(\vec{x}_i)\lambda_{m'}(\vec{x}_j)\mathrm{COV}(\hat{p}_m, \hat{p}_{m'}). \end{aligned} \tag{17}$$

It is noteworthy to mention that the measured line integral projection data at distinct detector elements and various view angles, representing different indices m and m', are statistically independent as long as the detector cross-talk effect can be neglected. Under this condition, we have $\mathrm{COV}(\hat{p}_m, \hat{p}_{m'}) = \delta_{mm'}\mathrm{var}(\hat{p}_m)$ and thus the above equation can be further simplified as follows:

$$C_{II}(\vec{x}_i, \vec{x}_j) = \sum_{m=1}^{M} \lambda_m(\vec{x}_i)\lambda_m(\vec{x}_j)\mathrm{var}(\hat{p}_m). \tag{18}$$

Note that it is the mathematical expectations are taken in the above formula to establish the relationship between the covariance of the CT image noise at two spatial locations and the covariance or variance of the projection data[9,23] at different view angles and detector elements labeled by a condensed index m.

In practice, one will have to estimate these quantities from experimental measurements. In this regard, the above relationships naturally gives us a method to estimate noise covariance and variance from projection data as follows:

$$\begin{aligned} \widehat{C_{II}}(\vec{x}_i; \vec{x}_j) &= \sum_{m,m'=1}^{M} \lambda_m(\vec{x}_i)\lambda_{m'}(\vec{x}_j)\widehat{\mathrm{COV}}(\hat{p}_m, \hat{p}_{m'}), \\ &= \sum_{m=1}^{M} \lambda_m(\vec{x}_i)\lambda_m(\vec{x}_j)\widehat{\mathrm{var}}(\hat{p}_m) \end{aligned} \tag{19}$$

When K repeated data acquisitions are performed, one can estimate the covariance of projection data from the measured projection data as follows:

$$\widehat{\mathrm{COV}}(\hat{p}_m, \hat{p}_{m'}) = \frac{1}{K}\sum_{\ell=1}^{K} \Delta\hat{p}_m^{(\ell)}\Delta\hat{p}_{m'}^{(\ell)} = \delta_{mm'}\widehat{\mathrm{var}}(\hat{p}_m). \tag{20}$$

Here, the superscript $(\cdot)^{(\ell)}(\ell = 1, \ldots, K)$ denotes the result from the ℓ-th independent CT data acquisition and $\widehat{\mathrm{COV}}(\hat{p}_m, \hat{p}_{m'})$ is the estimated covariance of the projection data represents the estimated variance of the line integral projection data $\hat{p}_m$ from K repeated measurements:

$$\widehat{\mathrm{var}}(\hat{p}_m) = \frac{1}{K}\sum_{\ell=1}^{K} \left[\Delta\hat{p}_m^{(\ell)}\right]^2. \tag{21}$$

To summarize, we have the following projection-domain local NPS measurement method:

$$\widehat{\mathrm{NPS}}(\vec{k}, \vec{x}_1) = \int_{\Delta\vec{x}\in\mathrm{ROI}} d(\Delta\vec{x})\, \widehat{C_{II}}(\vec{x}_1, \vec{x}_1 + \Delta\vec{x})e^{-2\pi i\vec{k}\cdot\Delta\vec{x}}. \tag{22}$$

In other words, as long as the covariance is estimated from the measured projection data using Equations (19)–(21), the local NPS can be readily estimated using the above windowed Fourier transform.

2.3 | Image-domain method to estimate covariance $C_{II}(\vec{x}_1, \vec{x}_2)$

To experimentally measure the NPS, whether for time-varying signals or spatially-varying signals, the crux is to estimate the auto-covariance in the temporal domain, as demonstrated in Equation (1), or in the spatial domain, as presented in Equation (11). When data acquisitions are repeated K times under identical conditions, the mathematical expectations are approximated from the corresponding sample averages as follows[32,33]:

$$\mathbf{E}[I(\vec{x}_1)] \approx \bar{I}(\vec{x}_1) = \frac{1}{K}\sum_{j=1}^{K} I^{(j)}(\vec{x}_1); \tag{23}$$

$$C_{II}(\vec{x}_1, \vec{x}_2) \approx \widehat{C}_{II}(\vec{x}_1, \vec{x}_2) = \frac{1}{K}\sum_{j=1}^{K} \Delta I^{(j)}(\vec{x}_1)\Delta I^{(j)}(\vec{x}_2), \tag{24}$$

where $\Delta I^{(j)}(\vec{x}) = I^{(j)}(\vec{x}) - \bar{I}(\vec{x})$. Here and throughout the paper, the approximated values for the mathematical expectations derived from measured experimental samples are denoted as $\widehat{(\cdot)}$, that is, by a wide hat above the corresponding quantities. Similar to the projection-domain method shown in Equation (22), upon taking the Fourier transform concerning the variable $\Delta\vec{x}$, the corresponding local NPS, centered around the pivotal point $\vec{x}_1$, can be inferred from the experimental samples as follows:

$$\begin{aligned} \widehat{\mathrm{NPS}}(\vec{k}, \vec{x}_1) &= \widehat{C}_{II}(\vec{k}, \vec{x}_1) \\ &= \int_{\Delta\vec{x}\in\mathrm{ROI}} d(\Delta\vec{x})\widehat{C}_{II}(\vec{x}_1, \vec{x}_1 + \Delta\vec{x})e^{-2\pi i\vec{k}\cdot\Delta\vec{x}}. \end{aligned} \tag{25}$$

When the image-domain estimation of the covariance $\widehat{C}_{II}(\vec{x}_1, \vec{x}_2)$ shown in Equation (24) is combined with the above definition of local NPS, some straightforward algebraic manipulations yield the following result:

$$\begin{aligned}\widehat{\mathrm{NPS}}(\vec{k}, \vec{x}_1) &= \int_{\Delta\vec{x}\in\mathrm{ROI}} d(\Delta\vec{x})\, \widehat{C}_{II}(\vec{x}_1, \vec{x}_1 + \Delta\vec{x}) e^{-2\pi i\vec{k}\cdot\Delta\vec{x}}, \\ &= \frac{1}{K}\sum_{j=1}^{K} \Delta I^{(j)}(\vec{x}_1) e^{2\pi i\vec{k}\cdot\Delta\vec{x}_1} \\ &\quad \times \int_{\vec{x}_2\in\mathrm{ROI}} d(\vec{x}_2)\, \Delta I^{(j)}(\vec{x}_2) e^{-2\pi i\vec{k}\cdot\vec{x}_2}, \\ &= \frac{1}{K}\sum_{j=1}^{K} \Delta I^{(j)}(\vec{x}_1) e^{2\pi i\vec{k}\cdot\Delta\vec{x}_1}\, \mathrm{DFT}[\Delta I^{(j)}(\vec{x}_2)]. \end{aligned} \tag{26}$$

Unfortunately, this does not provide a straightforward method to estimate the desired local NPS, as proposed in the projection-domain method in this paper. However, as shown in the next subsection, when a spatial average over the anchor point location $\vec{x}_1$ is performed, the $\vec{x}_1$-dependent factors in the above equation become another DFT of the "noise-only" image. As a result, one naturally arrives at the ICRU recommended NPS measurement method shown in Equation (10).

2.4 | Relationship between the ICRU method and the proposed local NPS estimation method defined in Equation (25)

In this subsection, we will show that *the conventional NPS measurement method depicted in Equation* (10), *is a spatial average of the point-wise NPS defined in Equation* (25) *over an ROI with an area of A*.

Utilizing the basic definition of Fourier transform, Equation (10) can be expressed as follows:

$$\begin{aligned}\widehat{\mathrm{NPS}}^{\mathrm{ICRU}}\left(\vec{k}\right) &= \frac{1}{AK}\sum_{k=1}^{K}\left|\mathrm{FT}_{2\mathrm{D}}[\Delta\hat{I}^{(k)}(\vec{x})]\right|^2 \\ &= \frac{1}{AK}\sum_{k=1}^{K}\left[\mathrm{FT}_{2\mathrm{D}}[\Delta\hat{I}^{(k)}(\vec{x})]\right]^*\left[\mathrm{FT}_{2\mathrm{D}}[\Delta\hat{I}^{(k)}(\vec{x})]\right] \\ &= \frac{1}{AK}\sum_{k=1}^{K}\left[\int_{\vec{x}_i\in\mathrm{ROI}} d\vec{x}_i\, e^{i2\pi\vec{k}\cdot\vec{x}_i}\Delta\hat{I}^{(k)}(\vec{x}_i)\right] \\ &\quad \times\left[\int_{\vec{x}_j\in\mathrm{ROI}} d\vec{x}_j\, e^{-i2\pi\vec{k}\cdot\vec{x}_j}\Delta\hat{I}^{(k)}(\vec{x}_j)\right] \\ &= \frac{1}{A}\int_{\vec{x}_i\in\mathrm{ROI}} d\vec{x}_i\, e^{i2\pi\vec{k}\cdot\vec{x}_i}\int_{\vec{x}_j\in\mathrm{ROI}} d\vec{x}_j\, e^{-i2\pi\vec{k}\cdot\vec{x}_j} \\ &\quad \times\left[\frac{1}{K}\sum_{k=1}^{K}\Delta\hat{I}^{(k)}(\vec{x}_i)\Delta\hat{I}^{(k)}(\vec{x}_j)\right]. \end{aligned} \tag{27}$$

Observe that the term in the square bracket in the last line is essentially the experimental estimation of image covariance $\widehat{C}_{II}$ between two points $\vec{x}_i$ and $\vec{x}_j$) as demonstrated in Equation (24). Consequently, the aforementioned equation can be reformulated into the following form:

$$\begin{aligned}\widehat{\mathrm{NPS}}^{\mathrm{ICRU}}\left(\vec{k}\right) &= \frac{1}{A}\int_{\vec{x}_i\in\mathrm{ROI}} d\vec{x}_i \\ &\quad \times\int_{\Delta\vec{x}\in\mathrm{ROI}} d(\Delta\vec{x}) e^{-i2\pi\vec{k}\cdot\Delta\vec{x}}\widehat{C}_{II}\left(\vec{x}_i; \vec{x}_i + \Delta\vec{x}\right) \\ &= \frac{1}{A}\int_{\vec{x}_i\in\mathrm{ROI}} d\vec{x}_i\, \widehat{\mathrm{NPS}}\left(\vec{k}, \vec{x}_i\right), \end{aligned} \tag{28}$$

where point-wise estimate of the NPS, that is, $\widehat{\mathrm{NPS}}\left(\vec{k}, \vec{x}_i\right)$, is defined in Equation (25). Clearly, the result above establishes that *the conventional NPS estimation method recommended by ICRU is simply the spatial average of the point-wise estimation proposed in this work*, $\widehat{\mathrm{NPS}}\left(\vec{k}, \vec{x}_i\right)$, *over the designated ROI*.

2.5 | Caveats in the ICRU-recommended image domain NPS measurement method

Based on Equation (28), the core concept of the ICRU-recommended NPS measurement approach, given multiple CT acquisitions, entails taking the spatial average of the point-wise NPS over a designated ROI. The estimated point-wise NPS from multiple CT acquisitions, denoted as $\widehat{\mathrm{NPS}}\left(\vec{k}, \vec{x}_i\right)$, is the Fourier transform of the estimated noise covariance, $\widehat{C}_{II}\left(\vec{x}_i; \vec{x}_j\right)$, which is estimated from the reconstructed images using data from multiple CT acquisitions as follows:

$$\begin{aligned}\widehat{C}_{II}\left(\vec{x}_i; \vec{x}_j\right) &= \frac{1}{K}\sum_{k=1}^{K}\Delta\hat{I}^{(k)}(\vec{x}_i)\Delta\hat{I}^{(k)}(\vec{x}_j) \\ &= \sum_{m,m'=1}^{M}\lambda_m(\vec{x}_i)\lambda_{m'}(\vec{x}_j)\widehat{\mathrm{COV}}(\hat{p}_m, \hat{p}_{m'}), \\ &= \sum_{m=1}^{M}\lambda_m(\vec{x}_i)\lambda_m(\vec{x}_j)\widehat{\mathrm{var}}(\hat{p}_m) \\ &\quad + \sum_{m\neq m'=1}^{M}\lambda_m(\vec{x}_i)\lambda_{m'}(\vec{x}_j)\hat{O}_{mm'}. \end{aligned} \tag{29}$$

Here $\widehat{\text{var}}(\hat{p}_m)$ is the variance of the projection data defined in Equation (21) and the term $\hat{O}_{mm'}(m \neq m')$ stands for the off-diagonal contribution:

$$\hat{O}_{mm'} = \frac{1}{K}\sum_{\ell=1}^{K} \Delta\hat{p}_m^{(\ell)} \Delta\hat{p}_{m'}^{(\ell)}. \tag{30}$$

Therefore, when it is compared with the projection domain estimation method shown in Equation (19), the image domain estimation method adopted by the ICRU recommendation included the off-diagonal contributions $\hat{O}_{mm'}$. It is the inclusion of this term in the estimation method that makes the estimated NPS with higher level of uncertainty as it is shown by the statistical properties of this off-diagonal term.

It is noteworthy to mention that the measured line integral projection data at distinct detector elements and various view angles, representing different indices m and m', are statistically independent as long as the detector cross-talk effect can be neglected. This leads us to the ensuing uncomplicated statistical attribute for the off-diagonal term $\hat{O}_{mm'}(m \neq m')$:

$$\begin{aligned}\mathbf{E}[\hat{O}_{mm'}] &= \frac{1}{K}\sum_{\ell=1}^{K} \mathbf{E}\left[\Delta\hat{p}_m^{(\ell)} \Delta\hat{p}_{m'}^{(\ell)}\right] \\ &= \frac{1}{K}\sum_{\ell=1}^{K} \mathbf{E}\left[\Delta\hat{p}_m^{(\ell)}\right]\mathbf{E}\left[\Delta\hat{p}_{m'}^{(\ell)}\right] = 0.\end{aligned} \tag{31}$$

In this equation, the fact $\mathbf{E}\left[\Delta\hat{p}_m^{(\ell)}\right] \equiv 0$ and statistical independence are employed. Similarly, the zero-mean result in the above equation is combined with the statistical independence for different data acquisitions denoted by the index ℓ and different detector element and view angle index m to obtain the variance of $\hat{O}_{mm'}$ as follows:

$$\text{var}[\hat{O}_{mm'}] = \mathbf{E}\left[\frac{1}{K}\sum_{\ell=1}^{K} \Delta\hat{p}_m^{(\ell)} \Delta\hat{p}_{m'}^{(\ell)}\right]^2 = \frac{1}{K}\text{var}[\hat{p}_m]\text{var}[\hat{p}_{m'}]. \tag{32}$$

A detailed derivation of the above result is presented in the Appendix.

2.6 | Summary: ICRU recommended method versus the proposed local NPS estimation method

In this work, we studied the relationship between the conventional NPS measurement method and the proposed local NPS measurement method. This work demonstrates that these two different methods become equivalent as long as the NPS is studied over an ROI selected in the conventional NPS definition. However, the new method enables local NPS measurement without the need for either stationarity or ergodicity conditions, which are often difficult to satisfy in practice. The key points are summarized as follows:

- First, the proposed method allows for local NPS measurement, starting with the estimation of the covariance $\widehat{C_{II}}(\vec{x}_i, \vec{x}_j)$, using the estimated variance of the projection data, that is, $\widehat{\text{var}}(\hat{p}_m)$. In contrast, the conventional NPS measurement method begins with the reconstructed image from each CT data acquisition, and these images are then used to estimate NPS by imposing additional assumptions of stationarity and ergodicity on the involved stochastic processes.
- Second, the conventional NPS estimation represents a spatially averaged local NPS, $\widehat{\text{NPS}}(\vec{k}, \vec{x}_i)$, over the entire selected ROI.
- Third, the conventional NPS measurement method shown in Equation (10) includes a term dictated exclusively by the variance of projection data $\widehat{\text{var}}(\hat{p}_m)$, and an additional zero-mean uncertainty term as shown in Equation (29). It is this zero-mean uncertainty term that hinders a precise estimate of NPS when the number of acquisitions, K, is small, as it contributes only measurement noise.

3 | EXPERIMENTAL VALIDATION METHODS

In this section, experimental measurements were conducted to validate the key findings of this paper, as summarized in the three bullet points in Section 2.6. To ensure a fair comparison of the NPS measurement results from the proposed local NPS projection-domain measurement methods and the conventional ICRU-adopted image-domain method, the exact same set of repeated photon counting detector PCD-CT projection data was used.

To avoid overlap, the data acquisition system and system geometry are identical to those presented in our co-pending paper.[52] For completion and clarity, here is a brief summary of the phantom and data acquisition parameters used in this work.

3.1 | Data acquisition parameters to characterize detector temporal and spatial correlations

Given the assumption that temporal and spatial correlation effects are negligible in the proposed local NPS measurement methods, it is imperative to validate this assumption within the context of the photon counting detector utilized in our validation studies. Experimental data were acquired through air scans under specific conditions: a tube voltage of 120 kV and a current of 240 mAs, identical to those used in local NPS measurements. A sequence of 1210 repeated frames was

captured consecutively at a rate of 0.1 s per frame (equivalent to 10 frames per second), to compile an ensemble of spatial and temporal dataset. Raw count data were recorded at a native resolution of 100 μm. The detector operated in anti-charge sharing mode with a low energy threshold of 23 keV to reject electronic noise.

Temporal and spatial correlation analyses (elaborated in subsequent subsections) were conducted on ROI encompassing 97 × 49 pixels, with each detector pixel measuring 0.1 mm × 0.1 mm. The 1210 frames of air scan data provided a time series with 1210 temporal data points for temporal correlation analysis, and equally 1210 samples for spatial correlation assessment.

3.2 | Temporal auto-correlations

To evaluate temporal lag behavior of the detector, the auto-correlation function (ACF) was analyzed across the temporal dimension for each detector element, utilizing the acquired data. This involved calculating the sample ACF, defined as:

$$R(\tau,\vec{x}) = \frac{1}{T}\sum_{t=1}^{T-\tau}\left(\frac{N(t,\vec{x})-\overline{N(\vec{x})}}{\sigma_N(\vec{x})}\right)\left(\frac{N(t+\tau,\vec{x})-\overline{N(\vec{x})}}{\sigma_N(\vec{x})}\right), \tag{33}$$

where $\vec{x}$ denotes a spatial location on the 2D detector plane, t denotes the image frame index and $T = 1210$ denotes the total frames of acquired data, $N(t,\vec{x})$ denotes the output counts of a pixel at $\vec{x}$ from the t-th image frame, $\overline{N(\vec{x})}$ is computed by taking the average of $N(t,\vec{x})$ along the t-dimension, and $\sigma_N^2(\vec{x})$ represents the variance of $N(t,\vec{x})$ along the t-dimension. The mean, $R(\tau)$, and standard deviation of these temporal auto-correlations were computed across all detector elements labeled by $\vec{x}$ over the entire detector to characterize the lag behavior of the detector.

3.3 | Spatial auto-correlations

The assessment of spatial auto-correlations between different detector elements was conducted by evaluating the noise spatial correlation of our photon counting detector. This evaluation was accomplished by calculating the Pearson correlation coefficient, r, between two spatial locations on the 2D detector plane, as outlined below:

$$r(\vec{x}_0,\vec{x}_0+\Delta\vec{x}) = \frac{1}{M-1}\sum_{i=1}^{M}\left(\frac{N_i(\vec{x}_0)-\overline{N(\vec{x}_0)}}{\sigma_N(\vec{x}_0)}\right) \times\left(\frac{N_i(\vec{x}_0+\Delta\vec{x})-\overline{n(\vec{x}_0+\Delta\vec{x})}}{\sigma_N(\vec{x}_0+\Delta\vec{x})}\right), \tag{34}$$

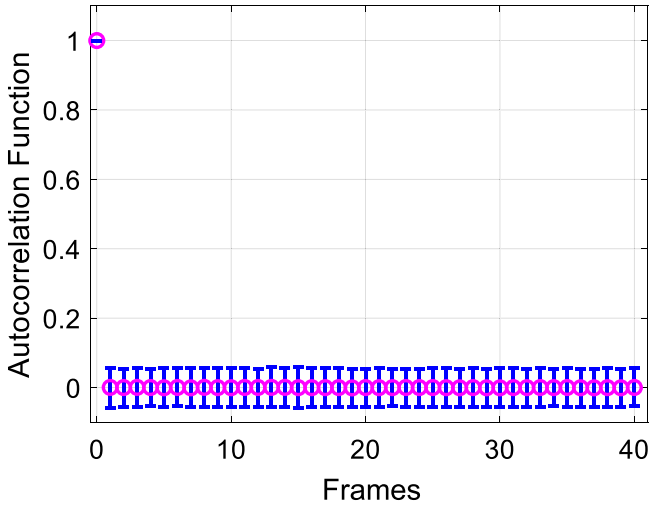

FIGURE 2 Temporal correlations across the detector panel for the first 40 shifted time points $\tau = 0, 1, \ldots, 40$ are presented. The time interval between successive points is determined by the detector's frame rate, which is equivalent to 100 ms for this study. The mean (denoted by a circle) and the 95% confidence interval are presented for each sampled τ value.

where $\vec{x}_0$ and $\vec{x}_0+\Delta\vec{x}$ denote two spatial locations on the detector plane. Here, $\vec{x}_0$ is considered an anchor point for the correlation coefficient calculation. $N_i(\vec{x}_0)$ represents the recorded counts of the pixel at $\vec{x}_0$ from the ith repeated measurement in the ensemble with a total of $M = 1210$ repeated time frames, $\overline{N(\vec{x}_0)}$ is the sample mean of $N_i(\vec{x}_0)$, and $\sigma_N(\vec{x}_0)$ denotes the sample variance of $N_i(\vec{x}_0)$.

3.4 | Phantoms and data acquisition parameters for local NPS measurements

To showcase the rich spatial variations of the local NPS measured using the proposed method in this paper, a relatively simple 16 cm-diameter uniform acrylic phantom was scanned using our benchtop PCD-CT system. Each photon counting CT scan was conducted at 120 kV and 240 mAs. The phantom underwent 100 repeated scans to implement the multi-acquisition NPS measurement method. The center of the acrylic phantom was precisely aligned with the iso-center of the photon counting CT system.

4 | EXPERIMENTAL RESULTS

This section showcases the experimental results to substantiate the theoretical insights discussed in this paper.

4.1 | Spatial and temporal correlations of detector counts

Figure 2 presents the correlation of detector outputs across different time frames within our experimental

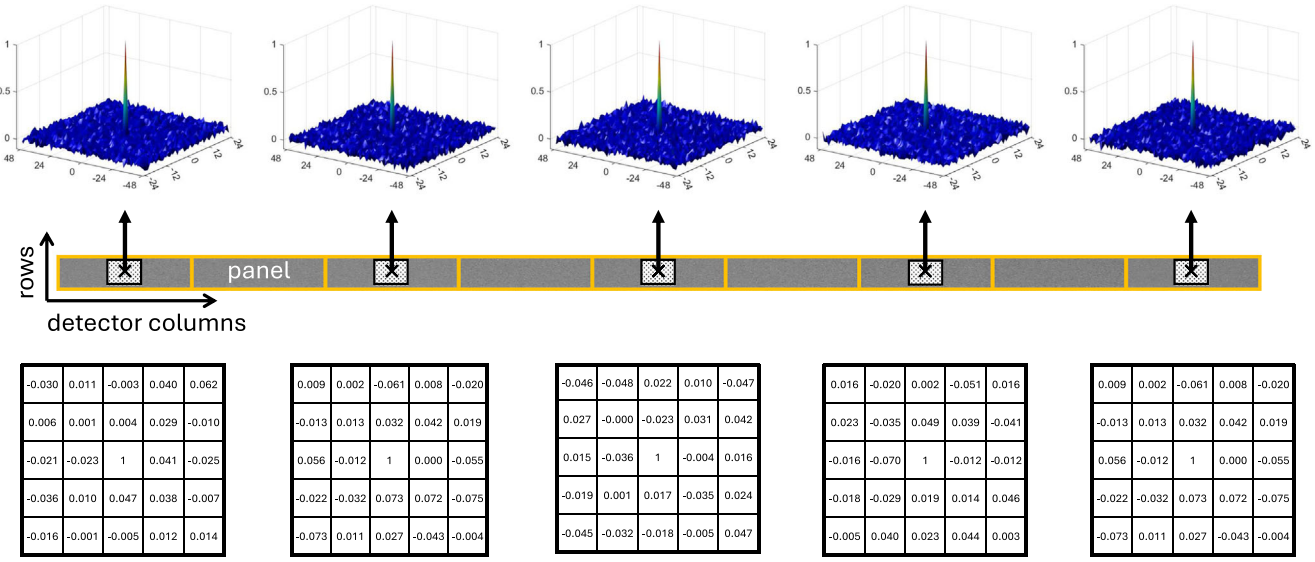

FIGURE 3 Spatial correlations of detector readout counts across five distinct ROIs. Data from these ROIs are sampled for presentation. Additionally, quantitative correlation values for these ROIs are presented, encompassing the 24 neighboring pixels centered around the pivot point. ROI, region of interest.

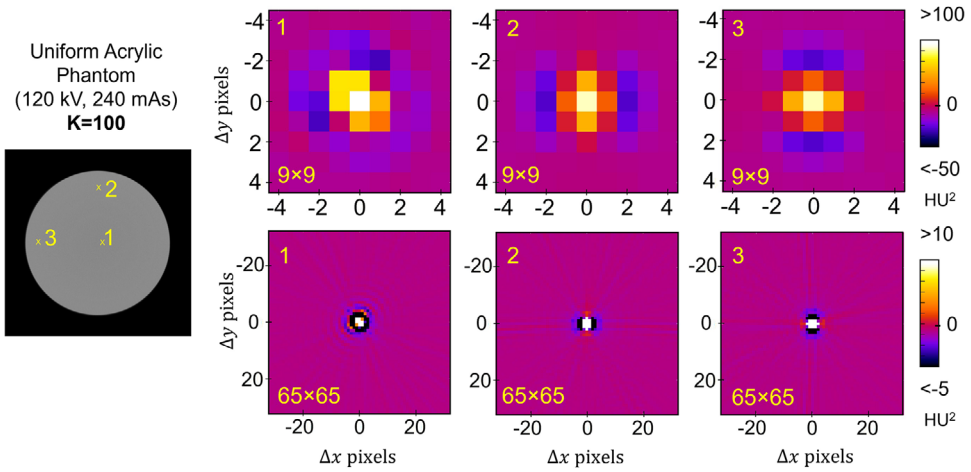

FIGURE 4 Covariance $\widehat{C}_{II}(\vec{x}_i, \vec{x}_j)$ was measured using the proposed projection-domain measurement method. ROIs of two different sizes (9 × 9 and 65 × 65) were centered at three points labeled on the image (locations 1, 2, and 3). ROI, region of interest.

data acquisitions. The correlation function $R(\tau)$ between different time frames, that is, $\tau \neq 0$, exhibits a zero mean. This observation suggests that the lag effect is negligible at a data acquisition rate of 10 frames per second.

Figure 3 presents the spatial correlation coefficients of detector outputs for five selected ROIs on the detector panel. The results indicate that spatial correlations among detector elements are minimal when the anti-charge sharing mode is enabled in our study.

4.2 | Covariance $\widehat{C}_{II}(\vec{x}_i; \vec{x}_j)$ using the proposed projection-domain method

Covariance $\widehat{C}_{II}(\vec{x}_i, \vec{x}_j)$ provides a quantitative characterization of the noise correlation between two locations $\vec{x}_i$ and $\vec{x}_j$. The spatial range of this correlation effect provides a good indication of the ROI sizes that enable the windowed Fourier transform to generate local NPS without significant spectral leakage. Figure 4 presents the measured $\widehat{C}_{II}(\vec{x}_i, \vec{x}_j)$ with $\vec{x}_i$ anchored at three

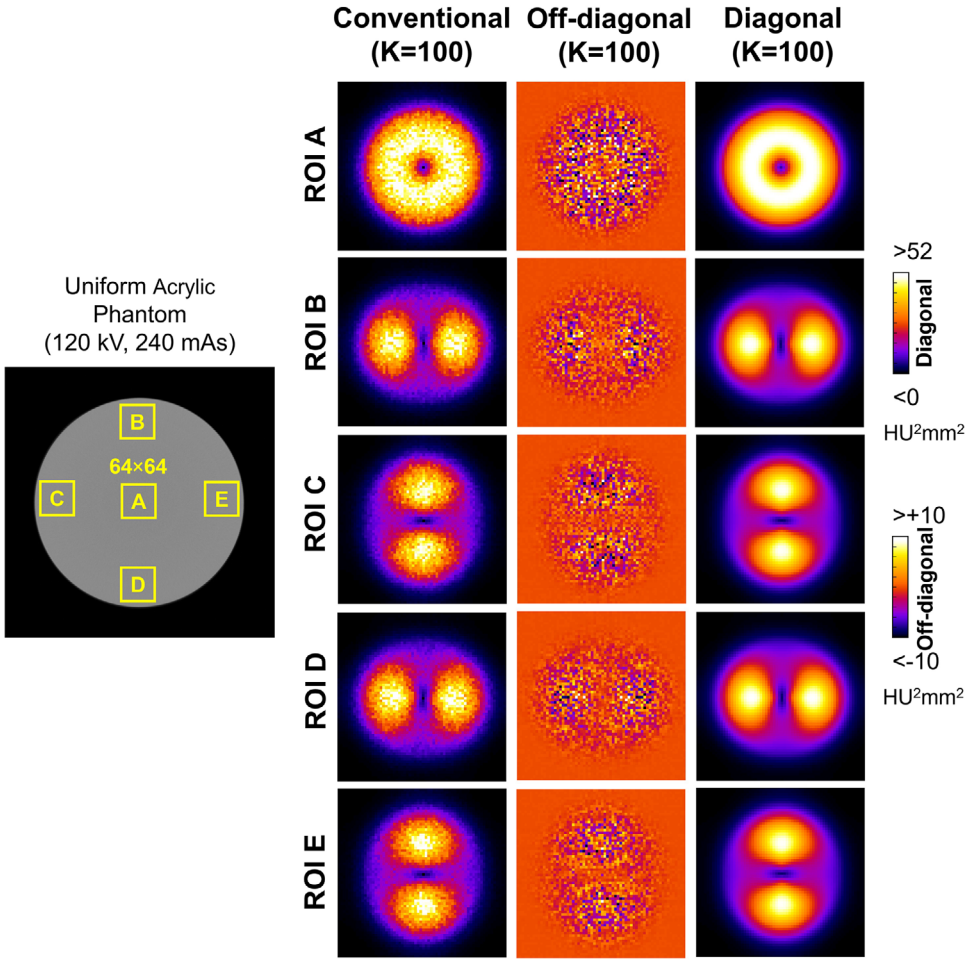

FIGURE 5 The conventional NPS measurement results (labeled as "Conventional") of the uniform acrylic phantom at five different ROIs with a pixel size of 64 × 64 are shown in the first column. The contribution from additional uncertainty (labeled as "Off-diagonal") is displayed in the second column. The contribution from the diagonal term is shown in the third column (labeled as "Diagonal"). NPS, noise power spectrum; ROI, region of interest.

different locations labeled on the reconstructed image and with two ROI sizes: 9 × 9 and 65 × 65. As shown in the results, the noise correlation estimated using the proposed projection-domain method is short-ranged. This indicates that one can accurately estimate local NPS by taking a DFT over a relatively small ROI, larger than 9 × 9.

4.3 | Conventional image-domain NPS measurement results: Diagonal contribution and additional uncertainty (off-diagonal) contribution

The conventional NPS measurement method, as shown by Equation (10), was used to measure the NPS at five different ROIs (four at the periphery and one at the center of the reconstructed image) in the uniform acrylic phantom. Each ROI has 64 × 64 image pixels. Results are presented in Figure 5. The NPS results in the first column are generated from the reconstructed images using the standard ICRU prescription (Equation (10)). Results in the second and third columns are the two contributing terms from Equation (29) are considered: the "Off-diagonal" term arises from the term $\hat{O}_{mm'}$ (Equation (30)) while the proposed method from the "Diagonal" contribution is generated from the estimated variance.

4.4 | Conventional Image-Domain NPS measurement: Averaged results of the proposed local NPS projection-domain measurement method

One of the central results in this work is presented in Equation (28). It elucidates the relationship between the proposed projection-domain local NPS measurement method and the conventional image-domain NPS measurement method: The result of the conventional NPS measurement is the spatial average of the proposed local NPS measurement method over the ROI. This relationship is illustrated in Figure 6: The result in

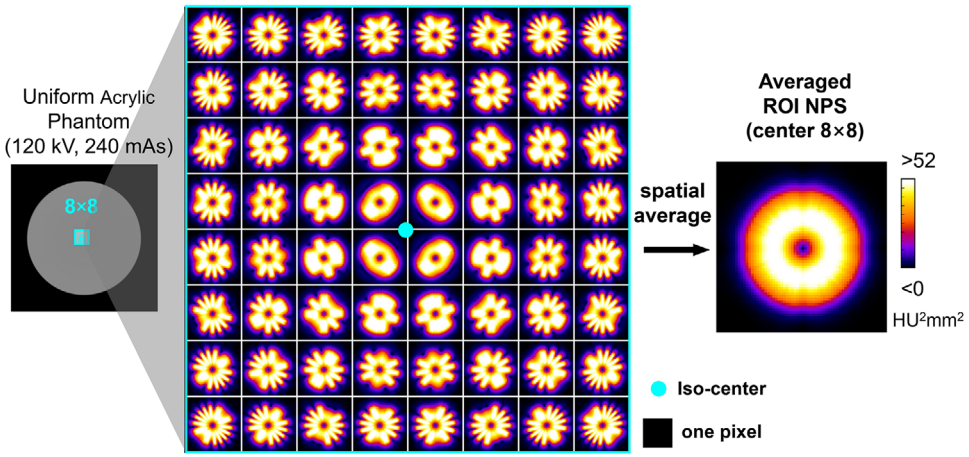

FIGURE 6 A detailed view of the NPS images contributed by the diagonal term in the conventional multi-acquisition approach is obtained by measuring at each pixel (point-wise) inside an 8 × 8 ROI at the iso-center. The NPS images obtained at each pixel within the ROI are then spatially averaged to form the "donut-shaped" ROI NPS. NPS, noise power spectrum; ROI, region of interest.

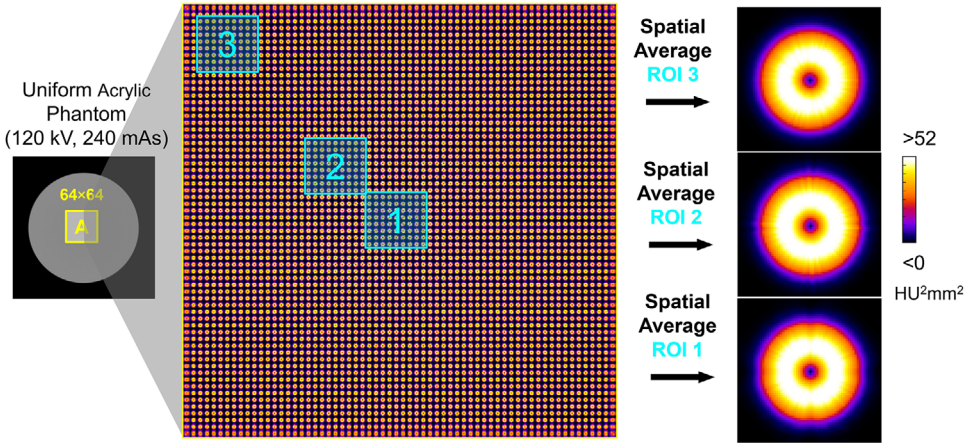

FIGURE 7 The ROI NPS images contributed by the diagonal term in the conventional multi-acquisition approach are obtained by taking the spatial average over three sub-ROIs (each with 8 × 8 pixels) within a larger ROI with 64 × 64 pixels. NPS, noise power spectrum; ROI, region of interest.

this figure displays the spatial average of the proposed local NPS measurement results over an ROI spanning 8 × 8 image pixels, generating the corresponding conventional NPS measurement of the diagonal term. (The results of the off-diagonal term will be presented in next subsection.) For simplicity, only the results for the ROI located at the center are presented.

The results in Figure 6 also indicate that for the chosen ROI of 64 image pixels, the proposed local NPS does not immediately reveal the well-known "donut-shape" NPS structure, which is almost circularly symmetric. Rather, the local NPS results reveal a rich NPS structure within the chosen ROI of 64 image pixels. Furthermore, the measured local NPS structures display a form of discrete rotational symmetry, with different rotation angles from the center to the periphery of the selected ROI. Once the spatial average is performed, the expected circular symmetry of the NPS structure emerges from the average of these local NPS measurements with discrete rotational symmetries.

Similar results are presented in Figure 7 for a larger ROI of 64 × 64 image pixels, illustrating the spatial average outcomes of these point-wise NPS measurements. The spatial averages are computed over three subsets drawn from 4096 local NPS results.

4.5 | Conventional NPS measurement results from multiple data acquisitions: Reducing uncertainty by increasing the number of data acquisitions

Figure 8 exhibits the variation in the off-diagonal term in the conventional NPS measurement method that employs multiple CT data acquisitions.

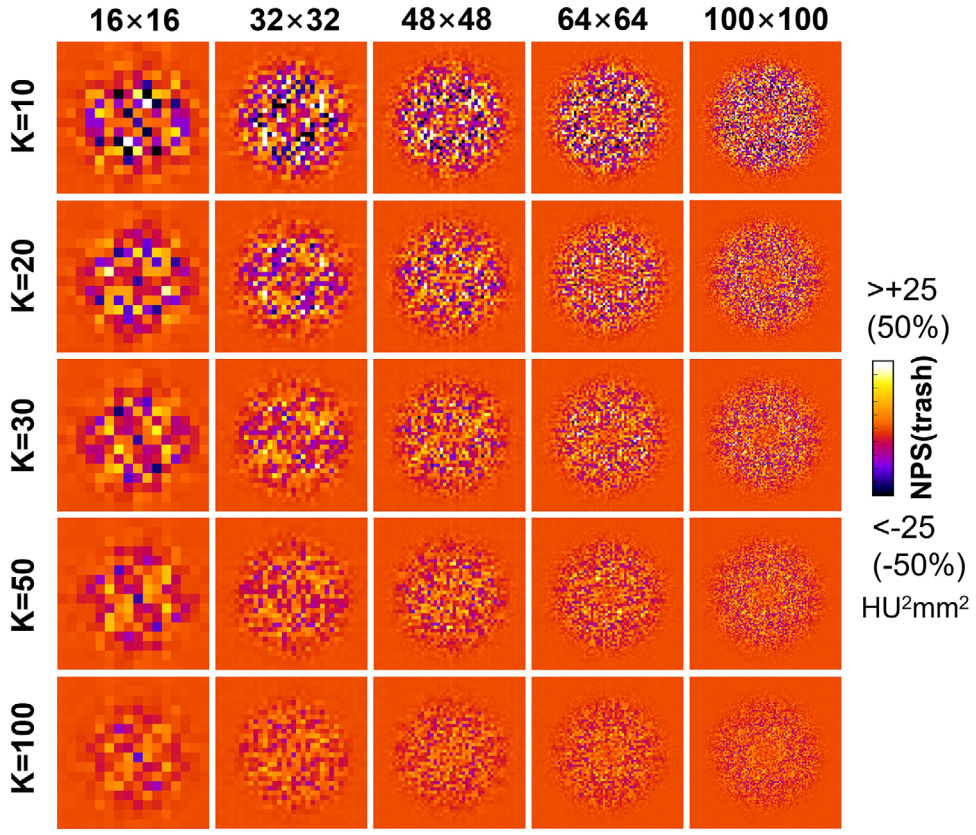

FIGURE 8 The variation of the uncertainty ("Off-diagonal") contribution in the conventional multi-acquisition NPS measurement method is analyzed with respect to the number of experimental collections (K) and the selected ROI size. The off-diagonal images exhibit noise-like characteristics, and the variation increases when fewer samples are acquired (in the row direction). Additionally, the off-diagonal images show similar variations across different ROI sizes due to the lower frequency resolution of the NPS image, which compensates for the smaller ROI size. NPS, noise power spectrum; ROI, regions of interest.

Within each row, at a fixed number of data acquisitions, the introduced off-diagonal term in the conventional NPS measurement displays a more spatially uniform noise distribution. In contrast, within each column, at a selected ROI size, the amplitude of the off-diagonal contribution added to the NPS measurement diminishes as the repetition number of data acquisitions increases.

The reduction in the added uncertainty of the off-diagonal term within the conventional NPS measurement method is quantified in Figure 9. It depicts a square root reduction correlated with the number of acquisitions.

4.6 | Root-causes of the rich structures in measured local NPS

The rich NPS structures presented in Figure 6 for a small 8 × 8 ROI and in Figure 6 for a larger ROI size of 64 × 64 are the new results of the proposed local NPS measurement method. The presence of these rich spatial variations in local NPS within the uniform acrylic phantom is rather unexpected. It turns out that the rich spatial structures of these local NPS are related to the interpolation weighting function $w(\theta;\vec{x})$, as explained in details in the Appendix II, used in image reconstruction and in the reconstruction of covariance from the corresponding variance of the projection data. To demonstrate this point, the geometrical contours $\eta(\theta;\vec{x})$ as functions of the polar angle θ are presented in Figure 10. These contours are overlaid over the corresponding local NPS results shown in Figure 6 to confirm that the shape of each local NPS matches these contours.

For better visualization, the contours and their corresponding local NPS results for the central column (D_1), central row (D_2), and off-diagonal line (D_3) are presented in Figure 11.

5 | DISCUSSION

This paper carried out theoretical analyses to elucidate the fundamental limitations of the widely-accepted image-domain NPS measurement method using multiple CT data acquisitions: The method is based on the assumption of both stationarity and ergodicity conditions, which are seldom satisfied[9,53] in experimental CT

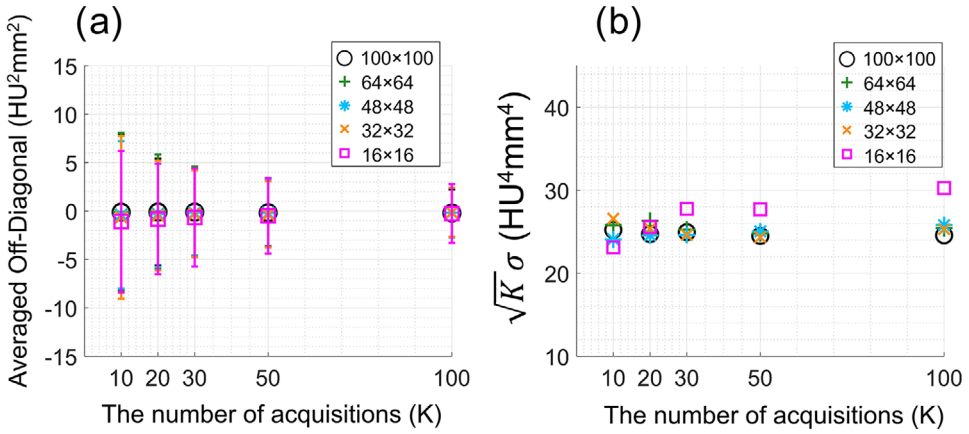

FIGURE 9 (a) The quantification of the off-diagonal images is shown in Figure 8, which displays the mean signal value across all the pixels in the measured NPS image. The error bars represent the standard deviation of the NPS image pixels. As the number of data acquisitions increases, the error bar decreases, while it remains approximately constant for different ROI sizes. (b) The normalized standard deviation is plotted against the number of data acquisitions in Figure 8, demonstrating a square root reduction of the error bar mentioned in sub-figure (a). NPS, noise power spectrum; ROI, regions of interest.

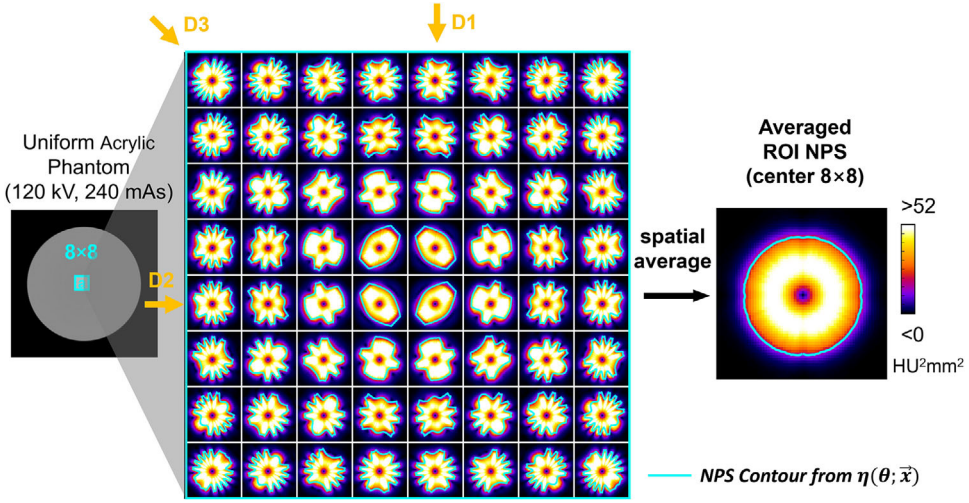

FIGURE 10 Contour profiles $\eta(\theta;\vec{x})$ with respect to the polar angle θ, as shown in Equation (B3), are overlaid on the local NPS to demonstrate that the shape of the local NPS is indeed determined by the contour profile function $\eta(\theta;\vec{x})$. NPS, noise power spectrum.

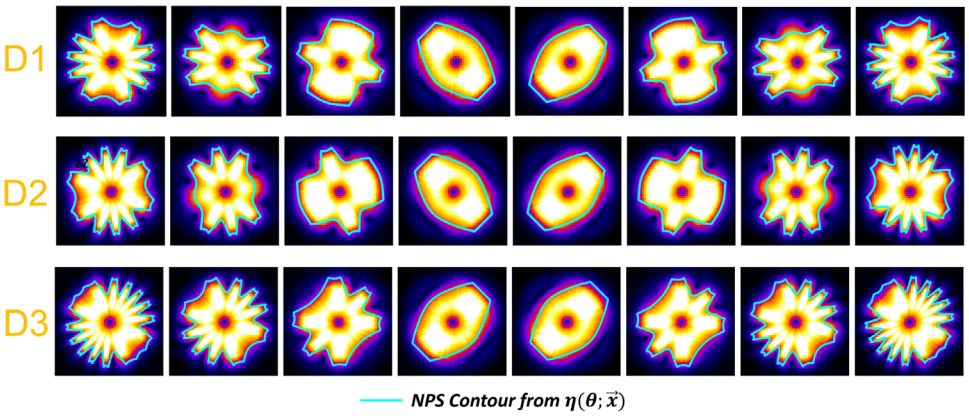

FIGURE 11 Zoomed-in contour profiles for three selected subsets of the local NPS: the central column (D_1), central row (D_2), and off-diagonal line (D_3). NPS, noise power spectrum.

data acquisitions. In that method, CT images are first reconstructed for each of the acquired CT datasets. The sample mean of the reconstructed images is then calculated and subtracted from the reconstructed image for each acquisition to produce the noise-only images. A Fourier transform is applied to the noise-only images before the modulus square of the Fourier transform is taken. In the final step, the sample average of these modulus square Fourier transforms is used to generate the NPS of the image.

In contrast, this work develops and validates a projection-domain local NPS measurement method. In this new method, one begins with the experimental estimation of the noise variance of projection data. A closed-form formula is then employed to calculate the corresponding experimental estimation of the noise covariance at any two locations, $\vec{x}_i$ and $\vec{x}_j$. The partial Fourier transform is subsequently taken with respect to a chosen anchor point $\vec{x}_i$ and their relative coordinates $\Delta\vec{x} = \vec{x}_j - \vec{x}_i$ to define local NPS at location $\vec{x}_i$.

The relationship between the local NPS defined in this work and the conventional image-domain NPS estimation method has been derived: it is the spatial average of the local NPS that yields the conventional NPS defined over the corresponding ROI.

Furthermore, due to the use of the sample mean to estimate the mathematical expectation of the image in generating the "noise-only" images in the conventional image-domain NPS measurement method, there is an additional off-diagonal term left in the conventional image-domain NPS measurement.[9,34] As a result, significant measurement uncertainties are introduced into the conventional image-domain NPS measurement method.

This work has the following potential limitations: First, the statistical independence assumption has been imposed on the proposed projection-domain local NPS measurement methods. However, in practice, this assumption can be violated, even in the context of PCD-CT imaging. For example, Tanguay et al.[54] investigated the impact of potential correlations on detective quantum efficiency (DQE) due to charge-sharing effects, while Xu et al.[55] examined these potential correlations when the anti-coincidence function of the detector is deactivated. Deactivating this function amplifies the spatial spread of the incident x-ray fluence across neighboring detector elements, enhancing their correlation. However, in practical applications, detectors are typically binned to either 0.2 mm $\times$ 0.2 mm for the so-called "ultra-high-resolution mode" (UHR) or 0.4 mm $\times$ 0.4 mm for the "high-resolution" mode in Siemens Naeotom Alpha PCD-CT scanners. This binning operation alleviates the charge-sharing induced detector spatial correlations, even with the anti-coincidence mode deactivated. In our study, the PCD operates in the anti-coincidence "ON" mode, and the low energy threshold is set at 23 keV. Under these conditions, we observed that the statistical independence assumption aligns well with the data acquisition conditions presented. That said, extra caution may be warranted when the proposed method is used in practice. For example, the anti-charge sharing mode might be deactivated when detecting high count rate x-ray fluence to counteract pulse pile-up.

Second, in this study, data acquisitions were conducted at a relatively low frame rate of 10 frames per second. At this frame rate, no temporal correlations were observed, as demonstrated in Figure 2. However, this observation is confined to a temporal interval of approximately 100 ms, indicating an absence of temporal correlation within this specific temporal scale. For future data acquisitions at frame rates higher than 10 frames per second, it will be necessary to investigate the presence and significance of temporal correlation effects.

Third, to produce high-precision and local NPS measurements using the proposed projection-domain method, access to line integral projection data, not just the reconstructed images, is needed. This could be a practical limitation since projection data are not typically available to end-users.

Fourth, in this work, we have exclusively discussed the local NPS measurement method using the filtered backprojection reconstruction method. However, one can readily apply this method to other reconstruction techniques, provided there exists a closed-form formula connecting image covariance with the corresponding noise variance of the projection data. In this context, it remains an open question to investigate the impact of the proposed method on other nonlinear image reconstruction methods, such as model-based iterative image reconstruction methods and more recent data-driven machine learning-based image reconstruction methods.

Furthermore, additional investigations are needed to extend the findings from photon counting CT to CT systems with energy-integrating detectors. For flat-panel energy-integrating detectors used in cone-beam CT imaging, factors such as detector lag[56] and afterglow may also challenge the statistical independence assumption imposed on the proposed local NPS measurement method. These limitations are beyond the current paper's scope and call for additional studies in the future.

6 | CONCLUSION

In conclusion, the conventional image-domain NPS measurement with multiple data acquisitions and reconstructed images only provides a spatially-averaged NPS estimate, and it unavoidably includes a term that only contributes measurement uncertainties instead of true NPS values. In contrast, the introduction of the projection-domain local NPS measurement method in this work uses the statistical estimator of the variance of the line integral projection data to measure noise

covariance and the consequent local NPS to reveal the rich structure variations in NPS.

ACKNOWLEDGMENTS

This work is partially supported by NIH through grants R01EB034011, R01EB032474, and R01HL153594. The work is also partially supported by GE Healthcare. One of the authors, Guang-Hong Chen, received partial support from the WARF Named Professorship, a chaired professorship bestowed by the University of Wisconsin-Madison's Office of the Vice Chancellor for Research and Graduate Education, with funding from the Wisconsin Alumni Research Foundation (WARF). Guang-Hong Chen extends sincere gratitude to Drs. Jeff Siewerdsen and Norbert Pelc for their stimulating and candid discussions, which greatly contributed to the development of this work.

CONFLICT OF INTEREST STATEMENT

The authors have no conflicts to disclose.

REFERENCES

1. Purcell EM, Morin DJ. Electricity and Magnetism. 3rd ed. Cambridge University Press; 2013.
2. Lathi BP, Green RA. Signal Processing and Linear Systems. Vol 2. Oxford University Press Oxford; 1998.
3. Schottky W. Über spontane Stromschwankungen in verschiedenen Elektrizitätsleitern. *Annalen Der Physik*. 1918;362:541-567.
4. Schottky W. On spontaneous current fluctuations in various electrical conductors. *Journal of Micro/Nanolithography, MEMS, and MOEMS*. 2018;17:041001-041001.
5. Johnson JB. Thermal agitation of electricity in conductors. *Phys Rev*. 1928;32:97.
6. Nyquist H. Thermal agitation of electric charge in conductors. *Phys Rev*. 1928;32:110.
7. Papoulis A, Unnikrishna Pillai S. Probability, Random Variables and Stochastic Processes. 4th ed. Tata McGraw-Hill; 2002.
8. Taylor GI. Diffusion by continuous movements. *Proceedings of the london mathematical society*. 1922;s2-20:196-212.
9. Barrett HH, Myers KJ. Foundations of Image Science. John Wiley & Sons; 2013.
10. Cunningham IA. Applied Linear-System Theory. Vol 1. chapter 2, SPIE Press; 2000:79-159.
11. Riederer SJ, Pelc NJ, Chesler DA. The noise power spectrum in computed X-ray tomography. *Phys Med Biol*. 1978;23:446.
12. Faulkner K, Moores B. Analysis of x-ray computed tomography images using the noise power spectrum and autocorrelation function. *Phys Med Biol*. 1984;29:1343.
13. Giger ML, Doi K, Metz CE. Investigation of basic imaging properties in digital radiography. 2. Noise Wiener spectrum. *Med Phys*. 1984;11:797-805.
14. Tapiovaara MJ, Wagner R. SNR and DQE analysis of broad spectrum x-ray imaging. *Phys Med Biol*. 1985;30:519.
15. Rabbani M, Shaw R, Van Metter R. Detective quantum efficiency of imaging systems with amplifying and scattering mechanisms. *JOSA A*. 1987;4:895-901.
16. Wilson DW, Tsui BM. Noise properties of filtered-backprojection and ML-EM reconstructed emission tomographic images. *IEEE Trans Nucl Sci*. 1993;40:1198-1203.
17. Siewerdsen JH, Antonuk LE, El-Mohri Y, et al,. Empirical and theoretical investigation of the noise performance of indirect detection, active matrix flat-panel imagers (AMFPIs) for diagnostic radiology. *Med Phys*. 1997;24:71-89.
18. Siewerdsen J, Cunningham I, Jaffray D. A framework for noise-power spectrum analysis of multidimensional images. *Med Phys*. 2002;29:2655-2671.
19. Pan X, Yu L. Image reconstruction with shift-variant filtration and its implication for noise and resolution properties in fan-beam computed tomography. *Med Phys*. 2003;30:590-600.
20. Zeng GL. Nonuniform noise propagation by using the ramp filter in fan-beam computed tomography. *IEEE Trans Med Imaging*. 2004;23:690-695.
21. Boedeker KL, Cooper VN, McNitt-Gray MF. Application of the noise power spectrum in modern diagnostic MDCT: part I. Measurement of noise power spectra and noise equivalent quanta. *Phys Med Biol*. 2007;52:4027.
22. Boedeker K, McNitt-Gray M. Application of the noise power spectrum in modern diagnostic MDCT: part II. Noise power spectra and signal to noise. *Phys Med Biol*. 2007;52:4047.
23. Wunderlich A, Noo F. Image covariance and lesion detectability in direct fan-beam x-ray computed tomography. *Phys Med Biol*. 2008;53:2471.
24. Yang K, Kwan ALC, Huang S-Y, Packard NJ, Boone JM. Noise power properties of a cone-beam CT system for breast cancer detection. *Med Phys*. 2008;35:5317-5327.
25. Tward DJ, Siewerdsen JH. Cascaded systems analysis of the 3D noise transfer characteristics of flat-panel cone-beam CT. *Med Phys*. 2008;35:5510-5529.
26. Tward DJ, Siewerdsen JH. Noise aliasing and the 3D NEQ of flat-panel cone-beam CT: effect of 2D/3D apertures and sampling. *Med Phys*. 2009;36:3830-3843.
27. Baek J, Pelc NJ. The noise power spectrum in CT with direct fan beam reconstruction. *Med Phys*. 2010;37:2074-2081.
28. Baek J, Pelc NJ. Local and global 3D noise power spectrum in cone-beam CT system with FDK reconstruction. *Med Phys*. 2011;38:2122-2131.
29. Baek J, Pelc NJ. Effect of detector lag on CT noise power spectra. *Med Phys*. 2011;38:2995-3005.
30. Pal D, Kulkarni S, Yadava G, Thibault B, Sauer K, Hsieh J. Analysis of noise power spectrum for linear and non-linear reconstruction algorithms for CT. In: 2011 IEEE Nuclear Science Symposium Conference Record. IEEE; 2011:4382-4385.
31. Zeng R, Petrick N, Gavrielides MA, Myers KJ. Approximations of noise covariance in multi-slice helical CT scans: impact on lung nodule size estimation. *Phys Med Biol*. 2011;56:6223.
32. IEC, Medical electrical equipment-characteristics of digital x-ray imaging devices - part 1-1: determination of the detective quantum efficiency-detectors used in radiographic imaging, international electrotechnical commission. IEC; 2015:62220-1-1.
33. International commission on radiation units and measurements, ICRU report no. 87: radiation dose and image-quality assessment in computed tomography. *J ICRU*. 2012;12:1-149.
34. Pineda AR, Tward DJ, Gonzalez A, Siewerdsen JH. Beyond noise power in 3D computed tomography: the local NPS and off-diagonal elements of the Fourier domain covariance matrix. *Med Phys*. 2012;39:3240-3252.
35. Solomon J, Samei E. Quantum noise properties of CT images with anatomical textured backgrounds across reconstruction algorithms: FBP and SAFIRE. *Med Phys*. 2014;41:091908.
36. Li K, Tang J, Chen G-H. Statistical model based iterative reconstruction (MBIR) in clinical CT systems: experimental assessment of noise performance. *Med Phys*. 2014;41:041906.
37. Lauzier PT, Chen G-H. Characterization of statistical prior image constrained compressed sensing. I. Applications to time-resolved contrast-enhanced CT. *Med Phys*. 2012;39:5930-5948.
38. Lauzier PT, Tang J, Chen G-H. Prior image constrained compressed sensing: implementation and performance evaluation. *Med Phys*. 2012;39:66-80.
39. Friedman SN, Fung GS, Siewerdsen JH, Tsui BM. A simple approach to measure computed tomography (CT) modulation transfer function (MTF) and noise-power spectrum (NPS) using

the American college of radiology (ACR) accreditation phantom. *Med Phys*. 2013;40:051907.
40. Melnyk R, Boudry J, Liu X, Adamak M. Anti-scatter grid evaluation for wide-cone CT. In: Medical Imaging 2014: Physics of Medical Imaging. Vol 9033. SPIE; 2014:778-784.
41. Gomez-Cardona D, Li K, Lubner MG, Pickhardt PJ, Chen G-H. Noise performance studies of model-based iterative reconstruction (MBIR) as a function of kV, mA and exposure level: impact on radiation dose reduction and image quality. In: Medical Imaging 2015: Physics of Medical Imaging. Vol 9412. SPIE Proceedings; 2015:801-807.
42. Zeng R, Gavrielides MA, Petrick N, Sahiner B, Li Q, Myers KJ. Estimating local noise power spectrum from a few FBP-reconstructed CT scans. *Med Phys*. 2016;43:568-582.
43. Schmitt SM, Goodsitt MM, Fessler JA. Fast variance prediction for iteratively reconstructed CT images with locally quadratic regularization. *IEEE Trans Med Imaging*. 2016;36:17-26.
44. Gomez-Cardona D, Li K, Hsieh J, Lubner MG, Pickhardt PJ, Chen G-H. Can conclusions drawn from phantom-based image noise assessments be generalized to in vivo studies for the nonlinear model-based iterative reconstruction method? *Med Phys*. 2016;43:687-695.
45. Gomez-Cardona D, Cruz-Bastida JP, Li K, Budde A, Hsieh J, Chen G-H. Impact of bowtie filter and object position on the two-dimensional noise power spectrum of a clinical MDCT system. *Med Phys*. 2016;43:4495-4506.
46. Cruz-Bastida JP, Gomez-Cardona D, Garrett J, Szczykutowicz T, Chen G-H, Li K. Modified ideal observer model (MIOM) for high-contrast and high-spatial resolution CT imaging tasks. *Med Phys*. 2017;44:4496-4505.
47. Hayes J, Gomez-Cardona D, Garrett J, Zhang R, Chen G-H. Noise and spatial resolution characteristics of unregularized statistical iterative reconstruction: an experimental phantom study. In: Medical Imaging 2018: Physics of Medical Imaging. Vol 10573. SPIE; 2018:777-783.
48. Li K, Chen G-H. CT image quality characterization. In: Computed Tomography (Editors: Samei and Pelc). Springer; 2020:85-124.
49. Wiener N. Generalized harmonic analysis. *Acta Math*. 1930;55:117-258.
50. Khintchine A. Korrelationstheorie der Stationären Stochastischen Prozesse. *Math Ann*. 1934;109:604-615.
51. Rice SO. Mathematical analysis of random noise. *Bell Syst Tech J*. 1944;23:282-332.
52. Zhang C, Li K, Zhang R, Chen G-H. Experimental measurement of local Noise Power Spectrum (NPS) in photon counting detector CT (PCD-CT) using a single data acquisition. *Med Phys*. Accepted (In Press) 2024.
53. Cunningham IA, Sattarivand M, Hajdok G, Yao J. Can a Fourier-based cascaded-systems analysis describe noise in complex shift-variant spatially sampled detectors? In: Medical Imaging 2004: Physics of Medical Imaging. Vol 5368. SPIE; 2004:79-88.
54. Tanguay J, Yun S, Kim HK, Cunningham IA. The detective quantum efficiency of photon-counting x-ray detectors using cascaded-systems analyses. *Med Phys*. 2013;40:041913.
55. Xu J, Zbijewski W, Gang G, et al,. Cascaded systems analysis of photon counting detectors. *Med Phys*. 2014;41:101907.
56. Siewerdsen J, Jaffray D. Cone-beam computed tomography with a flat-panel imager: effects of image lag. *Med Phys*. 1999;26:2635-2647.

How to cite this article: Zhang C, Li K, Zhang R, Chen G-H. Noise power spectrum (NPS) in computed tomography: Enabling local NPS measurement without stationarity and ergodicity assumptions. *Med Phys*. 2024;51:4655–4672. https://doi.org/10.1002/mp.17112

APPENDIX A: DERIVATION OF THE OFF-DIAGONAL TERM $\hat{O}_{mm'}$

This appendix presents the derivation of the off-diagonal term $\hat{O}_{mm'}(m \neq m')$ in Equation (32):

$$\begin{aligned}
\mathrm{var}[\hat{O}_{mm'}] &= \mathbf{E}\left[\frac{1}{K}\sum_{\ell=1}^{K}\Delta\hat{p}_m^{(\ell)}\Delta\hat{p}_{m'}^{(\ell)}\right]^2, \\
&= \frac{1}{K^2}\sum_{\ell,\ell'=1}^{K}\mathbf{E}\left[\Delta\hat{p}_m^{(\ell)}\Delta\hat{p}_{m'}^{(\ell)}\Delta\hat{p}_m^{(\ell')}\Delta\hat{p}_{m'}^{(\ell')}\right], \\
&= \frac{1}{K^2}\sum_{\ell=\ell'=1}^{K}\mathbf{E}\left[\Delta\hat{p}_m^{(\ell)}\Delta\hat{p}_{m'}^{(\ell)}\Delta\hat{p}_m^{(\ell')}\Delta\hat{p}_{m'}^{(\ell')}\right] \\
&\quad + \frac{1}{K^2}\sum_{\ell\neq\ell'=1}^{K}\mathbf{E}\left[\Delta\hat{p}_m^{(\ell)}\Delta\hat{p}_{m'}^{(\ell)}\Delta\hat{p}_m^{(\ell')}\Delta\hat{p}_{m'}^{(\ell')}\right], \\
&= \frac{1}{K^2}\sum_{\ell=1}^{K}\mathbf{E}\left[\left(\Delta\hat{p}_m^{(\ell)}\right)^2\left(\Delta\hat{p}_{m'}^{(\ell)}\right)^2\right] \\
&\quad + \frac{1}{K^2}\sum_{\ell\neq\ell'=1}^{K}\mathbf{E}\left[\Delta\hat{p}_m^{(\ell)}\Delta\hat{p}_{m'}^{(\ell)}\right]\mathbf{E}\left[\Delta\hat{p}_m^{(\ell')}\Delta\hat{p}_{m'}^{(\ell')}\right].
\end{aligned}$$

Using statistical independence for different data acquisitions labeled by the superscript index ℓ, the expectations are carried out to obtain the results as follows:

$$\begin{aligned}
\mathrm{var}[\hat{O}_{mm'}] &= \frac{1}{K^2}\times K\times\mathbf{E}\left[(\Delta\hat{p}_m)^2(\Delta\hat{p}_{m'})^2\right] \\
&\quad + \frac{1}{K^2}\times K(K-1)\times\mathbf{E}[\Delta\hat{p}_m\Delta\hat{p}_{m'}].
\end{aligned}$$

Once again, using statistical independence for the measurements at different detector and view angle labeled by the subscript index m, the results can be further simplified as follows:

$$\begin{aligned}
\mathrm{var}[\hat{O}_{mm'}] &= \frac{1}{K^2}\times K\times\mathbf{E}\left[(\Delta\hat{p}_m)^2\right]\mathbf{E}\left[(\Delta\hat{p}_{m'})^2\right] \\
&\quad + \frac{1}{K^2}\times K(K-1)\times\mathbf{E}[\Delta\hat{p}_m]\mathbf{E}[\Delta\hat{p}_{m'}], \\
&= \frac{1}{K}\mathrm{var}[\hat{p}_m]\mathrm{var}[\hat{p}_{m'}].
\end{aligned}$$

where the fact of $\mathbf{E}[\Delta\hat{p}_m] \equiv 0$ and $\mathbf{E}\left[(\Delta\hat{p}_m)^2\right] = \mathrm{var}[\hat{p}_m]$ are used in the final step.

APPENDIX B: CONTOURING PROFILE $\eta(\theta;\vec{x})$ OF THE LOCAL NPS

In FBP reconstruction of image $\hat{I}(\vec{x})$, the acquired projection data array at each view angle is first filtered using the ramp filter or its modified version, depending on the detector geometry. These filtered data at each view angle form a new array of the filtered data. To

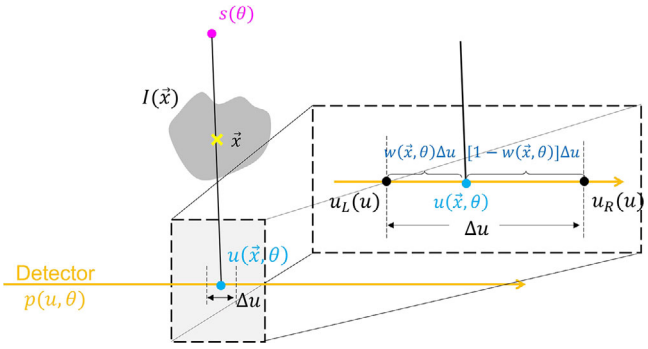

FIGURE B1 The geometrical illustration of the weighting factor $w(\theta;\vec{x})$.

reconstruct the image value at location $\vec{x}$, that is, $\hat{I}(\vec{x})$ as shown in Equation (14), the pixel-driven backprojection approach requires data interpolations to obtain the corresponding filtered data for the given ray passing through the targeted image point at location $\vec{x}$, as illustrated in Figure B1.

In our work, a linear interpolation scheme is employed with the following weighting function $w(\theta;\vec{x})$:

$$w(\vec{x};\theta) = \frac{u(\vec{x};\theta) - u_L[u(\vec{x};\theta)]}{\Delta u} \tag{B1}$$

where $u(\theta;\vec{x})$ denotes the position where the incident x-ray passing through $\vec{x}$ hits the detector. The function u_L identifies the most adjacent left detector pixel position to $u(\theta;\vec{x})$, and Δu represents the detector pixel size. This weighting function is included in the factor $\lambda_m(\vec{x})$ in Equation (14). As a result of this linear data interpolation scheme, the following factors appear in the estimated covariance $\widehat{C_{ll}}(\vec{x}_i;\vec{x}_j)$ in Equation (19):

$$\eta'(\theta;\vec{x}) = w^2(\vec{x};\theta) + [1 - w(\vec{x};\theta)]^2. \tag{B2}$$

Moreover, for each point $\vec{x}$, due to data redundancy in fan-beam data acquisition, a conjugate ray at $\theta + \pi$ contributes to the same image point $\vec{x}$. As a result, the final factors that appear in the estimated covariance $\widehat{C_{ll}}(\vec{x}_i;\vec{x}_j)$ in Equation (19) are given by:

$$\eta(\theta;\vec{x}) = \frac{1}{2}\left[\eta'(\theta;\vec{x}) + \eta'(\theta+\pi;\vec{x})\right]. \tag{B3}$$

This results in an angular-dependent profile of the covariance $\widehat{C_{ll}}(\vec{x}_i;\vec{x}_j)$ centered around the anchor point $\vec{x} = \vec{x}_i$. After applying the discrete Fourier transform to obtain the corresponding local NPS centered around $\vec{x} = \vec{x}_i$, this angular-dependent profile automatically results in an angular-dependent profile in the measured local NPS using the proposed projection-domain approach.